Unraveling the oxidation kinetics through electronic structure regulation of MnCo_2O_4.5@Ni_3S_2 p-n junction for urea-assisted electrocatalytic activity

Sangeeta Adhikari, Stephan N. Steinmann, Maheswari Arunachalam, Soon Hyung Kang, Do-heyoung Kim

Unraveling the oxidation kinetics through electronic structure regulation of $MnCo_2O_{4.5}$@Ni_3S_2 p-n junction for urea-assisted electrocatalytic activity

Sangeeta Adhikari[a], *Stephan N. Steinmann*[b]*, *Maheswari Arunachalam*[c], *Soon Hyung Kang*[c], *Do-Heyoung Kim*[a]*

[a]*School of Chemical Engineering, Chonnam National University, 77, Yongbong-ro, Buk-gu, Gwangju 61186,* Republic *of Korea*

[b]*Ecole Normale Supérieure de Lyon, CNRS, Laboratoire de Chimie UMR 5182, 46 allée d'Italie, F-69364 Lyon, France*

[c]*Department of Chemistry Education, Chonnam National University, Gwangju 61186, Republic of Korea*

*Corresponding authors:
Professor Do-Heyoung Kim, kdhh@chonnam.ac.kr
Dr Stephan N. Steinmann, stephan.steinmann@ens-lyon.fr

Abstract

A promising strategy to boost electrocatalytic performance is via assembly of hetero-nanostructured electrocatalysts that delivers the essential specific surface area and also active sites by lowering the reaction barrier. However, the challenges associated with the intricate designs and mechanisms remain underexplored. Therefore, the present study constructs a p-n junction in a free-standing $MnCo_2O_{4.5}$@Ni_3S_2 on Ni-Foam. The space-charge region's electrical characteristics is dramatically altered by the formed p-n junction, which enhances the electron transfer process for urea-assisted electrocatalytic activity. The optimal $MnCo_2O_{4.5}$@Ni_3S_2 electrocatalyst resulted in greater OER electroactivity, delivering an overpotential of only 240 mV than pure systems. Remarkably, upon employing as UOR electrode the required potential decreases to 30 mV. The impressive performance of the designed catalyst is attributed to the enhanced electrical conductivity, greater number of electrochemical active sites, and improved redox activity due to the junction interface formed between p-$MnCo_2O_{4.5}$ and n-Ni_3S_2. There is strong indication that the in-situ formed extreme-surface NiOOH starting from Ni_3S_2 boosts the electrocatalytic activity by lowering the generation potential of the surface reconstructive active species. In consideration, this work presents a high-performance p-n junction design for broad use, together with a viable and affordable UOR electrocatalyst.

Keywords: Density functional theory, p-n junction, Urea-assisted oxidation reaction.

Introduction

Hydrogen is one of the cleanest sustainable energy carriers, which is critically needed to reduce fossil-fuel dependence and develop energy storage and conversion systems from other carbon-free renewable resources [1]. The reaction rate for the water splitting process is governed by the electron- and proton-transfer processes in the hydrogen evolution reaction (HER) and oxygen evolution reaction (OER), respectively, which are the half-cell reactions of the water splitting process. Unlike the one-electron involvement in HER, OERs undergo multiple charge-transfer processes that contribute to high overpotentials owing to the sluggish kinetics [2]. Thus, the development of more efficient OER electrocatalysts is a challenging task. Another interesting approach is to lower the operating potential via substituted oxidation reactions [3] using other components, such as methanol [4], urea [5], and hydrazine [6].

Among these, urea is the most promising material as it is inexpensive, and the thermodynamic requirement of the urea-assisted oxidation reaction (UOR: $CO(NH_2)_2 + 6OH^- \rightarrow 5H_2O + N_2 + CO_2 + 6e^-$) is 0.37 V, which is significantly lower than the theoretical thermodynamic potential requirement of the OER, i.e., 1.23 V versus RHE [7]. The process also has the potential to treat urea-containing wastewater while generating "green" hydrogen [8]. Furthermore, UOR avoids the natural (thermal) conversion of urea into ammonia, which is harmful to the environment, as ammonia is a greenhouse gas [9]. Since, urea oxidation is a six-electron transfer process, the kinetics of the UOR is also sluggish, similar to the OER; therefore, it is necessary to develop an efficient electrocatalyst system for increasing the reaction rate by lowering the energy barriers for the catalytic processes [10]. Spinel cobaltite is a popular class of electrocatalysts as it has multimetallic centers that provide active oxidation states and promote electron transfer in the electrocatalytic system. Among them, the variants of manganese cobalt oxides ($MnCo_2O_4$, $MnCo_2O_{4.5}$, and $CoMn_2O_4$) have attracted the interest of the research community as OER electrocatalysts [11]. Despite the abilities of Mn and Co to provide rich valence states, the electrochemical properties are not truly excellent, and investigations pertaining to these systems are underdeveloped in comparison to other metal-oxide systems, even though there is plenty of literature on their excellent supercapacitor performances. To further boost the electrochemical catalytic activity, multi-electrocatalyst's combination such as 3D $MnCo_2O_4$@CoS nanoarrays [12], $MnCo_2O_4$/h-boron nitride [13], and Co_3O_4@$MnCo_2O_{4.5}$ nanocubes [14] is proven to be beneficial for performance

enhancement. Recently, construction of p-n junction is reported to have synergistic effect reducing the reaction activation energy through electronic structure modulation [15]. One of the works interestingly reports p-n junction constructed out of p-type Co_3O_4 and n-type Ni_3S_2 over Ni-foam which leads to excellent UOR activity due to the properties evolved from interface engineering [16]. Nickel based electrocatalysts have been very proactive as UOR medium due to high electroactivity and stability, as beautifully comprehended by Ma et al.[17] To aid the above mentioned features, efficient nanostructure design can increase the material porosity that can speed up the mass transport further boosting the performance through more exposure of active sites.

From this perspective, p-n junction with oxide-sulfide interface is reported to be beneficial for the conductivity of the ultimate catalyst [12, 18]. The aforementioned reasons are the foundation to develop p-n junction electrocatalyst composed of a 1D/2D $MnCo_2O_{4.5}$@Ni_3S_2 electrode on a self-supported porous Ni-foam (NF) substrate. The p-n junction interface will have a space charge effect that will improve the electronic mass transfer and charge conduction properties improving the electrocatalytic performance. $MnCo_2O_{4.5}$@Ni_3S_2 electrocatalyst electrode displays potential OER activity thanks to the electron redistribution at the p-n junction interface, which benefits from the enhanced conductivity and high-density active sites. Exceptional improvement in electrocatalytic OER/UOR activity and strong stability can be realized with a low overpotential of 240/30 mV and a small OER Tafel slope of 43 mV/dec in 1 M KOH solution. To the best of our knowledge, this is a pioneering study on this hybrid material, which offers an innovative and effective approach to create inexpensive, transition-metal-based electrocatalysts for both OER and UOR while achieving exceptional stable performance.

Results and Discussion

To understand the formation of p-n junction and recognize the synergistic properties delivered by $MnCo_2O_{4.5}$@Ni_3S_2 electrocatalyst system, ultra-violet photoelectron spectroscopy (UPS) measurements, Mott-Schottky (M-S) plots (derived from electrochemical impedance spectroscopy, **Figure S2a, b**) and UV-visible spectroscopy measurements were carried out at first to determine the charge transfer properties and energy band alignment. According to the curve, $MnCo_2O_{4.5}$ is a typical p-type semiconductor, whereas Ni_3S_2 indicates being an n-type semiconductor. **Figure 1a** shows the UPS spectra of the pristine $MnCo_2O_{4.5}$ (MCO) and Ni_3S_2-3 cycles (NS3) electrocatalyst. The E_{cutoff} (cutoff edge of the high binding energy value) derived from UPS measurements for the

pristine MCO and NS3 is observed to be 16.47 eV and 17.10 eV, respectively. With respect to the He excitation energy, the work function (Φ) values are 4.75 and 4.12 eV for MCO, and NS3 as per the following equation: $\Phi = h\nu - (E_{cutoff} - E_f)$; where hν is the excited photon energy from He I_α (21.22 eV) [19], E_{cutoff} is the intercept of the baseline, and E_f is the Fermi level of the calibrated spectrometer equating to 0 eV (**Figure 1b**). Additionally, the valence band maximum was determined using an energy threshold near E_f to indicate the energetic level of the located charge carriers, and the positions were at 0.42 eV for MCO and 1.7 eV for NS3 (**Figure 1c**). Consequently, the Fermi level of MCO and NS3 are calculated to be located at -4.75 and -4.12 eV versus vacuum level. Based on the Fermi level values, the valence band positions of MCO and NS3 were obtained to be -5.17 and -5.82 eV versus vacuum, respectively. The energy band gap of both the materials were derived from the Tauc plot as shown in **Figure 1d (Figure S2c)**, which are 1.71 eV for MCO and 2.62 eV for NS3. The conduction band position is calculated to be -3.46 and -3.20 eV versus vacuum for MCO and NS3 correspondingly. Based on the above calculations, the energy diagram of both $MnCo_2O_{4.5}$ and Ni_3S_2-3 cycles is constructed. The E_f values of $MnCo_2O_{4.5}$ and Ni_3S_2 in noncontact circumstances clearly show a large difference. Due to the considerable E_f difference between $MnCo_2O_{4.5}$ and Ni_3S_2, which will produce a major energy-level shift, the $MnCo_2O_{4.5}$ and Ni_3S_2 p-n junction interface will form a strong space charge region upon close contact. Upon formation of space charge region at the $MnCo_2O_{4.5}$ and Ni_3S_2 p-n junction heterostructure interface, the electrons will be transported from n-type Ni_3S_2 to p-type $MnCo_2O_{4.5}$ until the E_f alignment resulting in band edge bending and energy-level shifting. In light of the foregoing, the self-driven electron transfer from Ni_3S_2 to $MnCo_2O_{4.5}$ will result in a local charge redistribution along the p-n junction interfaces, which will cause electron loss on the Ni_3S_2 side and electron gathering on the $MnCo_2O_{4.5}$ side. Just as expected, the active centers that are more potent and carry efficient positive charges will be established at the Ni_3S_2 side, and the electrons derived from OH- will accelerate transfer to the VB of Ni_3S_2 in alkaline electrolyte, thereby promoting the OER catalytic activity. To sum up, p-n junction electrocatalyst can benefit in enhanced charge transfer through the built-in electric field and enhance the electrocatalytic reaction kinetics exhibiting higher performance than traditionally developed electrocatalyst systems. The heterostructure-type architecture in the p-n junction electrocatalyst can help in expanding the active surface area that not only upgrades the active interfacial sites but also contributes to faster electrochemical reactions due to modulated electronic properties.

Figure 1g illustrates the detailed procedures for the synthesis of the one-dimensional (1D) $MnCo_2O_{4.5}$ nanotips electrocatalyst on NF and electrochemical growth of the two-dimensional (2D) Ni_3S_2 nanosheets with $MnCo_2O_{4.5}$ nanotips acting as the core. First, during the hydrothermal processing of the MnCo-precursor on NF, the hydrolysis of $CO(NH_2)_2$ produces OH^- and CO_3^{2-}, which combine with the available Co^{2+} and Mn^{2+} metal ions to form the MnCo- precursor having the nanotips morphology grown on NF, followed by annealing to obtain the $MnCo_2O_{4.5}$ nanotips. On the other hand, an ecofriendly electrodeposition technique was adopted to grow the Ni_3S_2 nanosheets at room temperature on both NF and 1D-MCO, in which the amounts of grown Ni_3S_2 were controlled by the electrodeposition cycles. The as-prepared electrocatalyst electrodes were used as the working electrocatalyst electrodes with an exposed geometric area of 1 × 1 cm^2.

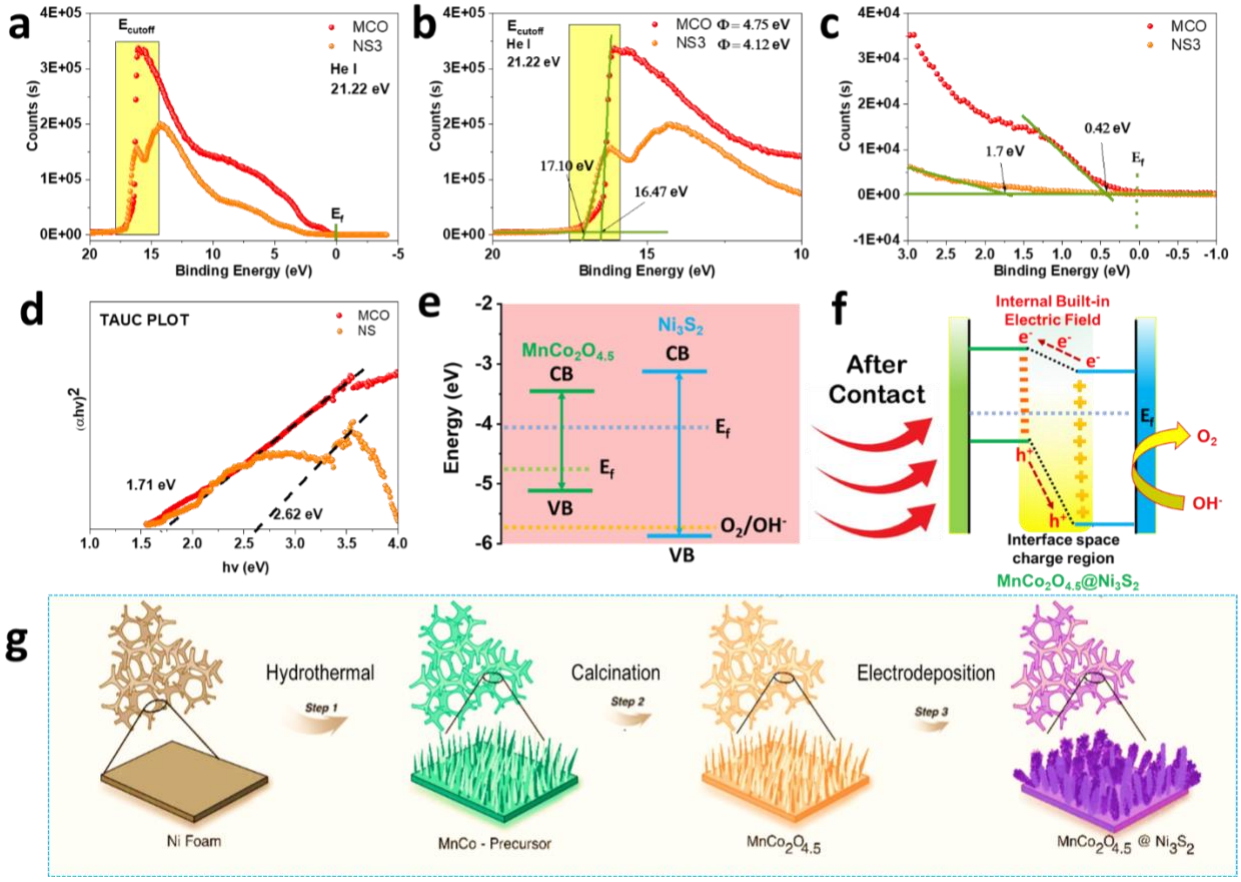

Figure 1. (a) Ultra-violet photoemission spectra (He I) of $MnCo_2O_{4.5}$ and Ni_3S_2, (b) the corresponding calculated work function (Φ) from the secondary electron cut off energy, (c) Energy threshold near Fermi level to derive the valence band maxima, (d) Tauc plot of $MnCo_2O_{4.5}$ and Ni_3S_2 using the UV-visible absorbance spectra, (e) Band energy diagram versus vacuum level of the p-type $MnCo_2O_{4.5}$ and n-type Ni_3S_2 before contact, (f) Formation of p-n junction between

$MnCo_2O_{4.5}$ and Ni_3S_2 after contact building an internal electric field promoting space charge transfer at interface zone, and (g) Schematic illustration of the fabrication of $MnCo_2O_{4.5}$ nanotips and p-n junction $MnCo_2O_{4.5}$@Ni_3S_2 architectures on Ni-foam substrate.

Initially, the crystal phases of the as-prepared electrodes were investigated by X-ray diffraction (XRD) measurements. In the diffraction patterns, the commonly observed sharp peaks at 44.6° and 51.9° are from the NF substrate (**Figure 2a**). From the XRD pattern of the grown $MnCo_2O_{4.5}$, the crystal phase is confirmed to be cubic (JCPDS No. 32-0297). Electrodeposition of Ni_3S_2 grown on the NF substrate or on $MnCo_2O_{4.5}$ does not affect the crystal phase of the core material, as can be seen in the XRD patterns (marked as ♣ in the MCONS3 sample), which confirms the absence of phase impurities. For reference, the XRD peak patterns obtained for Ni_3S_2 on NF for 1, 3, and 5 cycle numbers are shown in **Figure S3**. The poorly crystalline Ni_3S_2 exhibits heazlewoodite-phase (JCPDS No. 44-1418). The major peaks of both $MnCo_2O_{4.5}$ and Ni_3S_2 are observed to overlap with each other. The field-emission scanning electron microscopy (FESEM) and transmission electron microscopy (TEM) images demonstrate well hierarchical growth of Ni_3S_2 on $MnCo_2O_{4.5}$ on Ni-foam. The micrographs of the hydrothermally grown $MnCo_2O_{4.5}$ on NF substrate show 1D nanotip-like that are well interconnected, having vertical alignment on the NF (**Figure S4a, b and Figure 2d**). **Figure S4a'** displays the energy dispersive X-ray spectroscopy (EDS) of MCO and the obtained elemental composition is close to the weight ratios of elements approximately. In the MCONS3, the good structural alignment is maintained after Ni_3S_2 deposition, and shows 2D nanosheets over the nanotips, making it a core-shell-type architecture (**Figure 2b, c and Figure 2f, g**). For reference, Ni_3S_2 grown on $MnCo_2O_{4.5}$ for 1, 3 and 5 cycles are presented in **Figure S4f-h** along with Ni_3S_2 grown on NF at various cycles (**Figure S4c-e**). The HRTEM image in **Figure 2e** clearly shows the interplanar spacing to be 0.234 nm, which can be ascribed to the (222) plane arising from cubic crystal phase of the spinel $MnCo_2O_{4.5}$. In **Figure 2h**, the nanosheet edges are beautifully exposed, showing rough surface features and the inset shows the selected-area electron diffraction (SAED) pattern for the corresponding micrograph, revealing the polycrystalline nature of the prepared sample. The enlarged micrograph of the Ni_3S_2 nanosheet edge displays lattice fringes from the small particles on the nanosheet surface (marked in dotted line). These small particles are possibly Ni_3S_2 nuclei that self-assemble to form sheets during electrodeposition. The interspacings between the lattice fringes are measured to be 0.287 and 0.238 nm, matching with

the (110) and (003) crystal planes of Ni_3S_2, respectively (**Figure 2i**). The line scans obtained from scanning transmission electron microscopy (STEM) EDS analysis reveal the core to be composed of Mn, Co, and O, with distinct shelling from the Ni and S elements (**Figure 2j**). Additionally, the elemental distribution displays the elements Mn, Co, O, Ni, and S to have uniform distribution with high continuity for both the core and shell elements (**Figure 2k**).

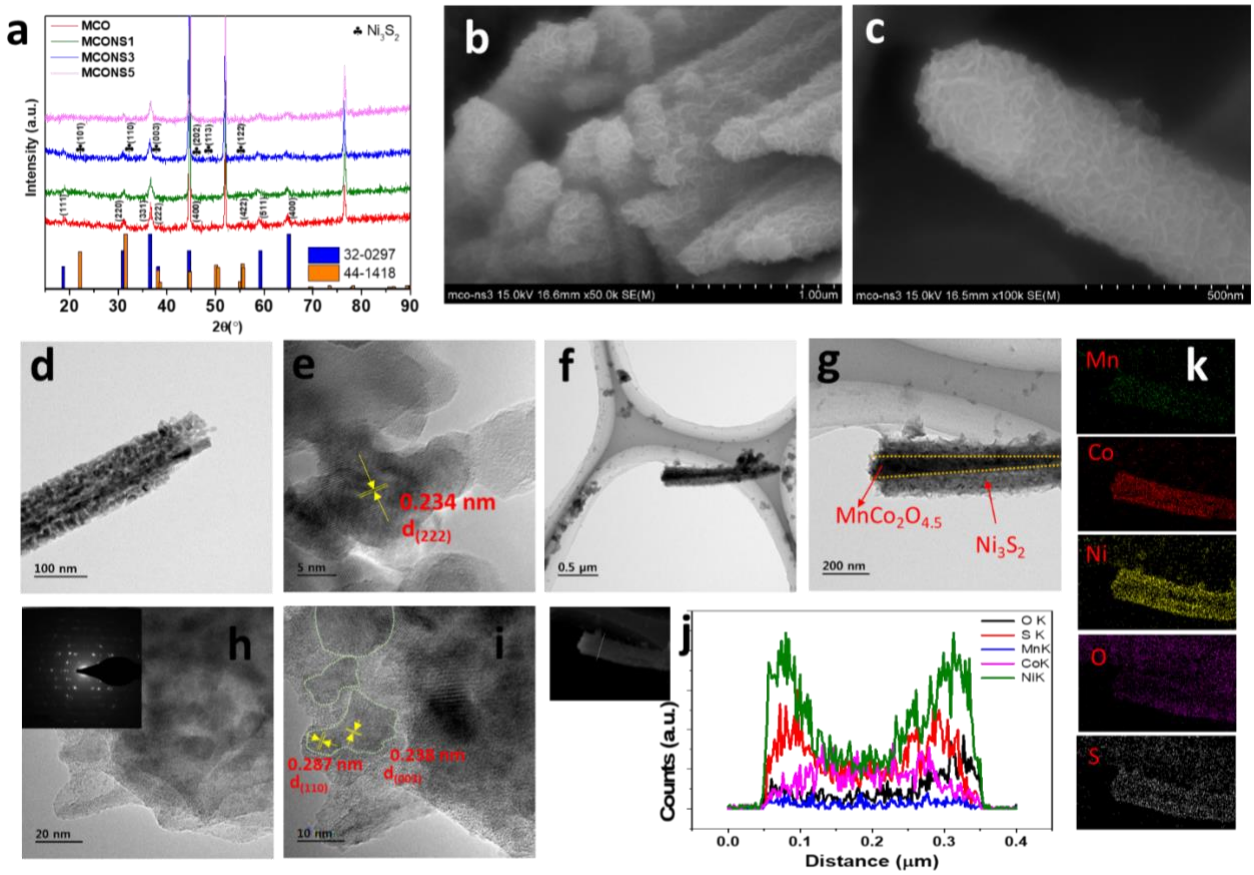

Figure 2. (a) X-ray diffraction patterns for the MCO, MCONS1, MCONS3, and MCONS5 electrodes; FESEM micrographs of (b-c) MCONS3. Typical TEM images of (d) MCO and (f-i) MCONS3 (h- inset shows the SAED pattern). HRTEM images of (e) MCO and (i) MCONS3. (j) STEM image and corresponding line scans, and (k) Elemental mapping micrographs of elements Mn, Co, O, Ni, and S in MCONS3 electrocatalyst.

The obtained Brunauer-Emmett-Teller (BET) surface areas are 9.9, 0.45, and 11.5 $m^2 g^{-1}$ for MCO, NS3, and MCONS3 with pore diameter of 10.2, 21.0 and 9.3 nm, respectively. As observed in the figure, MCO and MCONS3 exhibit type-IV isotherms, indicative of the materials possessing mesoporous characteristics (**Figure 3a**). The chemical compositions of the prepared

electrocatalysts were detected by XPS, and the surveys of all three samples are presented in **Figure S5.** The binding energies of the elements Mn, Co, Ni, O, and S are referenced using the 284.8 eV peak corresponding to the adventitious carbon C 1s [20]. The Mn 2p spectrum in MCO resolves into two spin-orbit doublets Mn $2p_{3/2}$ and Mn $2p_{1/2}$ at binding energies of 642.1 and 653.7 eV, respectively. The individual Mn $2p_{3/2}$/Mn $2p_{1/2}$ doublet spectrum can be deconvolved to three peaks at 640.3/652.9 eV, 642.1/653.7 eV, and 644.6/654.9 eV appearing from the Mn^{2+}, Mn^{3+}, and Mn^{4+} oxidation states of Mn, respectively, with a satellite peak (marked as Sat. in **Figure 3b**) observed at 647.4 and 656.2 eV [11a, 21]. However, there is a negative shift in binding energy of MCONS3, indicating charge distribution at the interface. For the Co $2p_{3/2}$ core spectrum in MCO (**Figure 3c**), the characteristic peaks at binding energies of 779.9 and 781.4 eV arise from the Co^{3+} and Co^{2+} states negatively shifting to 779.5 and 791.2 eV, respectively, after electrodeposition of Ni_3S_2. In the Ni 2p spectrum of NS3, the two small peaks at 853.0 and 870.5 eV arise from the Ni^0 from the spin doublets Ni $2p_{3/2}$ and Ni $2p_{1/2}$, respectively. A sharp Ni^{2+} peak is observed for both doublets with their corresponding satellite peaks. Similar peaks are also observed in MCONS3 with slight positive shifts. As per the O 1s XPS of MCO, the spectrum is deconvolved to three peaks, namely O1 (529.9 eV), O2 (531.0 eV), and O3 (532.1 eV), designated as metal-oxygen peaks arising from the oxygen in hydroxyl groups and from the adsorbed water molecules, respectively [22]. In contrary, the metal-oxygen bonds becoming weaker after Ni_3S_2 electrodeposition (**Figure 3e**) [23]. As shown in **Figure 3f**, the sulfur in Ni_3S_2 exhibits three deconvolved peaks, in which the main peaks appear at binding energies of 162.7 eV and 163.8 eV corresponding to S $2p_{3/2}$ and S $2p_{1/2}$, respectively. A satellite peak at 168.5 eV is also observed marked as Sat. in the figure. Fourier transformed EXAFS data for Mn, Co and Ni K-edge from MCONS3 are displayed in **Figure S5b-d**. Individual elemental foils are being used as standard reference. The major peak at 2.33 Å in Mn foil appears from Mn-Mn coordination which is missing in MCONS3 indicating atomic dispersion of Mn [24]. Peaks at 1.0 and 1.5 Å is due to Mn-O (from MnO_6 octahedra) and broad peaks at around 3.0 Å arises from the corner shared Mn [25]. It can be inferred that octahedral and tetrahedral sites in spinel are randomly occupied by Mn element [26]. The first contributions around 1.5 Å is the interatomic distance between Co ions and oxygen atoms possibly with a shoulder peak in left from Co scattering present at tetrahedral sites [27] [28]. Similar observations are found in Mn-based spinel ferrite systems [26]. The Ni EXAFS spectra in the K-edge shows main peak at 1.85 Å which is indicative of the Ni-S coordination with absence of Ni-

Ni (appears at around 2.18 Å) [29] and presence of oxides at lower radial distance at 1.5 Å (**Figure S5d**). Upon literature comparison, it could be believed that the Ni-S bonds in MCONS3 are shorter in comparison to pristine Ni_3S_2, which increases the Ni coordination number producing more Ni-S bonds [29-30].

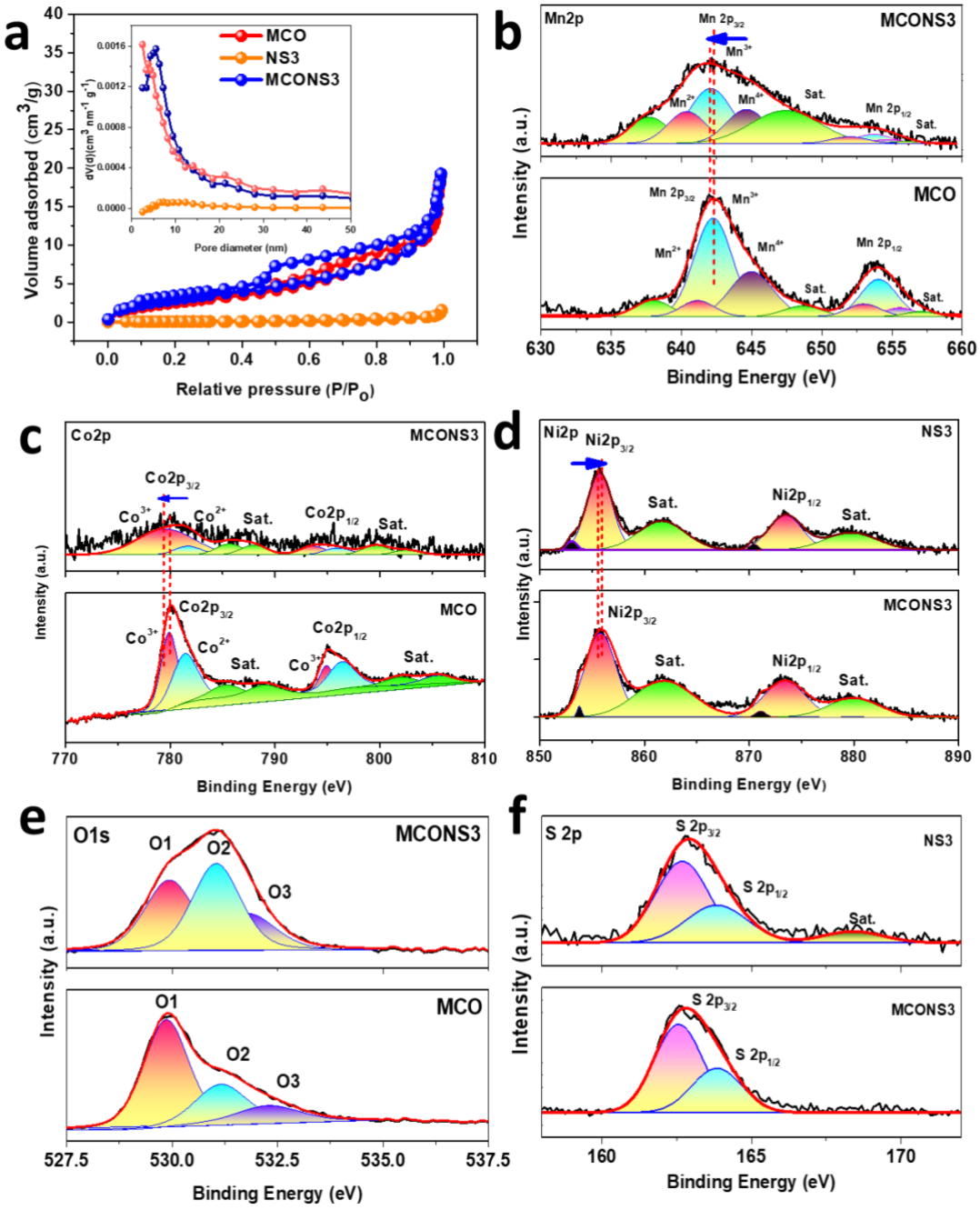

Figure 3. (a) Nitrogen adsorption–desorption isotherms of MCO, NS3, and MCONS3 (inset figure presents the corresponding pore-size distribution curves); high-resolution XPS data of (b) Mn 2p,

(c) Co 2p, and (d) O 1s in MCO and MCONS3; and high-resolution XPS data of (e) Ni 2p and (f) S 2p in NS3 and MCONS3.

The electrocatalytic activities of the as-prepared electrocatalyst are investigated using a three-electrode setup at room temperature in the presence of 1.0 M KOH aqueous electrolyte (**Figure 4a**). Since the CV curves for the forward bias exhibit surface oxidation peaks, backward CV curves were considered for calculating the overpotentials of the prepared electrocatalysts as per equations (1) and (2) given in supporting information. The p-n junction MCONS3 catalyst exhibits the best OER electrocatalytic activity with the smallest overpotential of 240 mV at a current density of 10 mA/cm^2. The obtained overpotential is much lower than those of the pristine MCO and NS3. It is worth mentioning that MCONS3 requires the lowest overpotentials of 240, 330, and 410 mV to reach 10, 50, and 100 mA/cm^2 current densities, as shown in **Figure S6a**. The MCONS3 also shows the smallest Tafel slope of 43 mV/dec compared to MCO and NS3 (**Figure 4b and 4c**). It is worth mentioning that with increase in the Ni_3S_2 nanosheets grown on the $MnCo_2O_{4.5}$ nanotips, the catalytic activity is hindered possibly owing to overgrowth resisting the charge-transfer pathways despite junction formation [31], which is evident from the increases in both overpotential and Tafel slope values. In general, the Tafel slope values are critical indicators of the types of catalytic mechanisms, followed by the electrocatalyst. In the present study, the Tafel slope values for MCONS3 is between 40 and 60 mV/dec, which is indicative of the O-O bond formation being the rate-limiting step during OER electrocatalysis [32]. Another important feature was to understand the optimized electrode's and electrolyte affinity to have a better picture of solid-liquid interaction. Thus, characteristics of the electrode surface was understood from the wettability behavior (contact angle measurement of a water droplet on the electrode's surface) , where comparison between bare Ni-foam and MCONS3 was conducted, and the recorded optical photographs are shown in **Figure S6b**. As observed in the images, the contact angle of the droplet on bare Ni-foam was about ≈114°, indicating hydrophobic property of Ni-Foam'surface. In contrast, the water droplet on MCONS3 electrode is quickly absorbed suggesting a superhydrophilic behavior of the electrode's surface. Such property is extremely beneficial in improvising the electrocatalytic performance. To further understand the enhanced electrochemical activity of MCONS3, the double-layer capacitance (C_{dl}) data were used to obtain the electrochemical surface areas (ECSAs). It is one of the important aspects that influences the electrocatalytic efficacy which is proportional to the magnitude of C_{dl}.

The corresponding ECSAs are 52, 70.75, and 168.75 per cm^2 for the NS3, MCO and MCONS3 electrocatalyst electrodes (**Figure S7 and Figure 4d**). The morphological evolution of the prepared electrocatalysts should also be the source of this increasing ECSA for MCONS3 electrocatalyst. These results prove that the Ni_3S_2 shell over $MnCo_2O_{4.5}$ has synergistic effects in improving the activity through the exposed active sites, as also confirmed from the BET and SEM results. An abundance of active sites and accelerated electron transfer could be provided by this kind of structural feature, improving the OER properties. To further support the results, EPR results of MCO and MCONS3 are reported in **Figure S7d** which very well shows that there is a synergy between MCO and NS3 in comparison to MCO. Although, the signal in MCO is characteristics of the oxygen vacancy in the system, but an increase in the characteristic intensity of MCONS3 suggests enhancement in the oxygen vacancy which could be the possible reason for promotion of the catalytic activity. The intrinsic activities were determined by normalizing the current densities with the obtained ECSA values (**Figure 4e**). The obtained intrinsic activity for MCONS3 is retained much higher than those of MCO and NS3 electrocatalyst electrodes after normalization. The intrinsic activity of the MCONS3 electrocatalyst is greatly increased by tuning the electronic structure more effectively through active interfacial sites by the use of such a 3-D architecture. To gain further insight into the catalytic properties, the mass activities of MCO, NS3, and MCONS3 were compared at an overpotential of 240 mV (1.47 V vs. RHE). As observed in **Figure 4f**, the mass activities of the electrocatalysts MCO, NS3, and MCONS3 at 1.47 V vs. RHE are 2.88, 3.17, and 8.92 A/g, respectively. The activity of MCONS3 is 3.09 and 2.81 times higher than those of MCO and NS3, respectively, suggesting that the Ni_3S_2 shell on $MnCo_2O_{4.5}$ enhances the interfacial active sites through the formed p-n junction interface which promotes the OER activity.

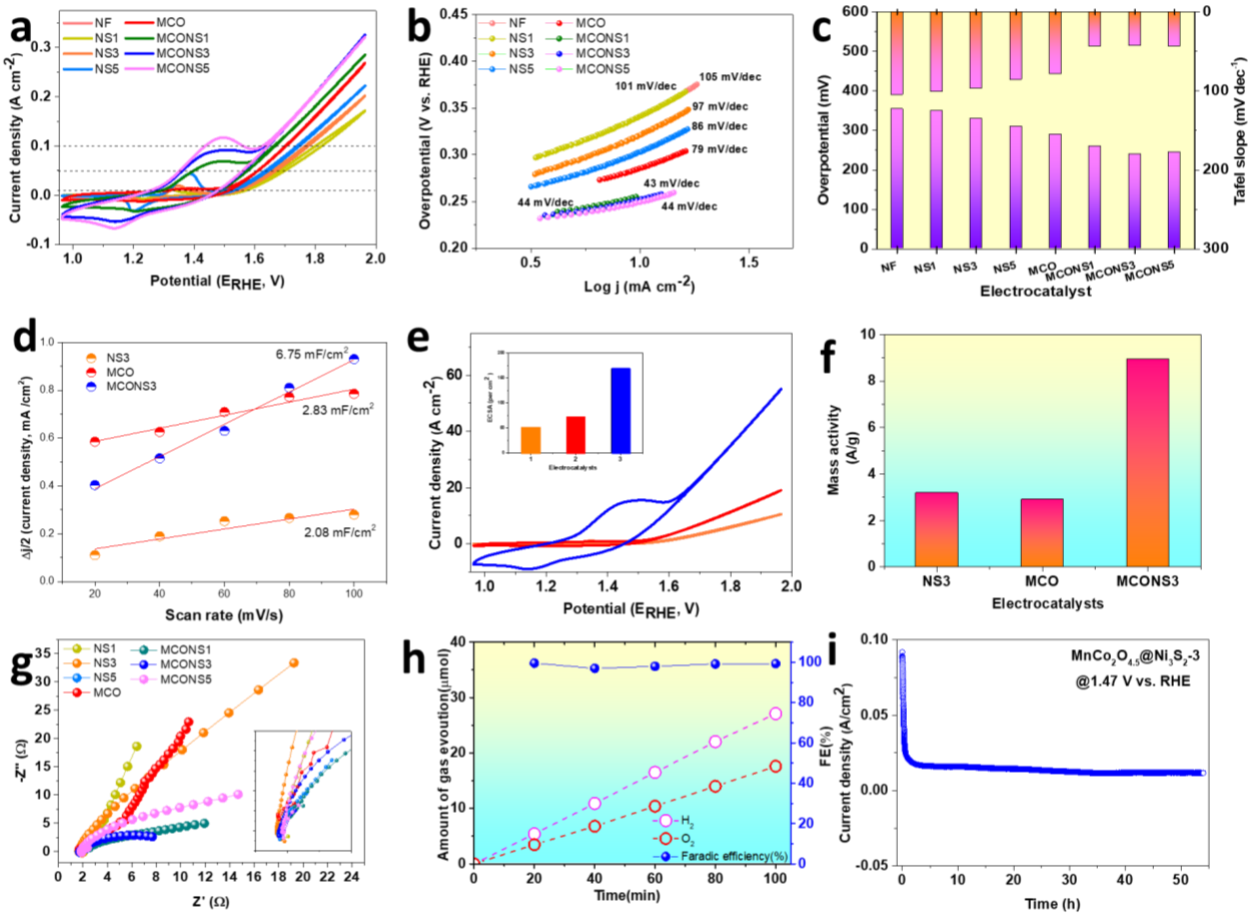

Figure 4. Electrocatalytic activities of various catalysts towards OER process measured in 1.0 M KOH electrolyte (without iR calibration). (a) Comparative CV curves of the NS, MCO, and MCONS catalyst series; (b) Tafel slopes corresponding to the CV curves in (a); (c) overpotential comparison at 10 mA/cm^2 and Tafel slopes obtained from (a) and (b); (d) capacitive Δj (Δj = j_a-j_c/2) versus the scan rates for the catalysts; (e) ECSA-normalized current densities (inset shows the corresponding ECSA values of 1.NS, 2.MCO, and 3.MCONS3); (f) Mass activities at an overpotential of 1.47 V vs. RHE; (g) Nyquist plots of all the prepared electrocatalyst electrodes; (h) comparison of calculated and experimentally measured oxygen and hydrogen gases and faradaic efficiencies; (i) stability tests of the MCONS3 electrocatalyst electrode towards OER.

The Nyquist plots (**Figure 4g**) display that the charge transfer resistance (R_{ct}) for MCONS3 was 8.01 Ω, which is much smaller than those of the other electrocatalysts representing faster charge transfer in the MCONS3 catalyst. Apart from the comparative study, Nyquist plots of optimized MCONS3 at different overpotentials can be the key in justification of OER kinetic process (**Figure**

S8a). As the overpotential rises, the impedance resistance arc shrinks meaning decrease charge-transfer resistance. Consequently, it is commonly accepted that the rate-determining step of OER processes is the relaxing of the adsorbed intermediates on the surface of the optimized electrocatalyst as also evident from the EIS results [33]. The oxygen and hydrogen gas evolution rates along with faradaic efficiency were measured using gas chromatography (**Figure 4h**). As observed, the amounts of H_2 and O_2 gas evolution rates at 20 mA/cm^2 current density were 28 and 16 µmol and that the faradaic efficiency was >98% during different reaction intervals. Surprisingly, the MCONS3 electrode exhibited excellent durability with negligible current decay for more than 50 h at 1.47 V vs. RHE, as presented in **Figure 4i**. The spent electrode shows a shift of about 20 mV in the CV curves with a near-identical shape of the curve (**Figure S8b**) indicating possible deterioration of the thin Ni_3S_2 nanosheets decreasing the accessible electroactive sites. The post-stability characterizations of MCONS3 electrode were carried out using FESEM, XRD and XPS (**Figure S9-S11**) which revealed that the morphology was well retained with no new diffraction peaks and all elements integrally present in the electrocatalyst. The MCONS3's performance was compared with other reported Mn, Co, Ni based oxide and sulfide systems (in **Table S1**).

The electrochemical UOR for the optimized electrocatalyst MCONS3 electrode was investigated in a three-electrode setup in 1 M KOH electrolyte with 0.33 M urea and compared with the OER performance (**Figure 5a**). The potential required to achieve 10 mA/cm^2 is 1.26 V vs. RHE, which is much smaller than the OER catalytic activity (1.47 V vs. RHE) and also in comparison to MCO and NS3 (**Figure S12**). It can be anticipated that the lower potential requirement for UOR favorably eases the electrochemical process at the anode in lieu of OER catalysis. The UOR electrocatalytic performance further increases with increasing molar concentration of the electrolyte to 6 M KOH, as observed in **Figure 5b**. For attaining a current density of 100 mA/cm^2, the potential required was 1.4 V vs. RHE. At the same potential, the current density achieved with 6 M KOH + 0.33 M urea was 480 mA/cm^2, which was Δ= 380 mA/cm^2 higher, satisfying the basic criterion for UOR industrial application. These results indicate that the UOR process can boost the production of energy-saving H_2 at relatively lower potentials. The differences in potentials for both UOR and OER processes are clearly evident in **Figure 5c**. For real-time implications, concentration-dependent studies were performed, which indicates that the current density increases with increase in urea concentration (**Figure 5d**). While the OH- ions are crucial to urea oxidation

events at the interface, they protect against CO poisoning brought on by these processes. Because of this, the electrode surface is automatically cleaned, thereby preventing surface CO fouling by conversion to CO_2 molecules. The influence of scan rates studies (**Figure S13)** reveal that the reduction peak current shows a potential shift almost linearly with respect to the scan rate, as have been observed in other material systems [34]. **Figure 5e** display a staircase voltage curve with respect to the current density under both UOR and OER conditions, and with each alteration in the current density, the potential becomes instantly flat and remains approximately stable for the rest of the duration. Furthermore, the long-term stability MCONS3 electrode under UOR processing was tested and evaluated by the multistep chronoamperometry method with applied potentials of 1.26, 1.32, and 1.41 V vs. RHE (**Figure 5f**). The prepared electrode showed unobvious fluctuations of ± 3, ± 5, and ± 7.5 mA/cm^2 current densities at the corresponding potentials, which implies excellent stability of the electrocatalyst electrode. The studies also demonstrate that the electrocatalyst is highly stable under alkaline conditions while delivering significant UOR performance. In addition, the amount of hydrogen evolved during the UOR electrochemical process was evaluated (**Figure 5g**), and the amount of hydrogen evolution was found to be 42 µmol at 20 mA/cm^2 current density, which is obviously greater than the H_2 produced by the OER process.

The post-characterizations (XRD, SEM, TEM, and XPS) for the spent MCONS3 electrode after 50 h of UOR process were conducted (**Figure S10, S14, S15 and Figure 5h**) reveals formation of a few nanometers of amorphous layer via TEM that could have formed owing to surface reconstruction and transformation into metal oxyhydroxide layer, likely NiOOH [35], which was later confirmed in XPS. The UOR performance of the prepared electrocatalyst MCONS3 electrode is also compared with other reported Mn, Co, and Ni based oxide and sulfide systems (**Figure 5i**), which show that the present overpotential outperforms most of the UOR electrocatalysts (the electrochemical activity details are summarized in **Table S2**). Finally, a full cell experiment with MCONS3 || MCONS3 was conducted and the operating voltage required overall water splitting is about 1.49 V to reach current density of 10 mA/cm^2, whereas 1.28 V with the same current density is required for urea electrolysis, respectively. By using constant current rates of 50 mA/cm^2, the cell voltage of 1.65 and 1.49 eV was achieved initially, which increased to 1.70 and 1.51 V, after 50 h of electrochemical water splitting and urea electrolysis, respectively as shown in the chronopotentiometry examination (**Figure S16**) indicating excellent durability with negligible loss.

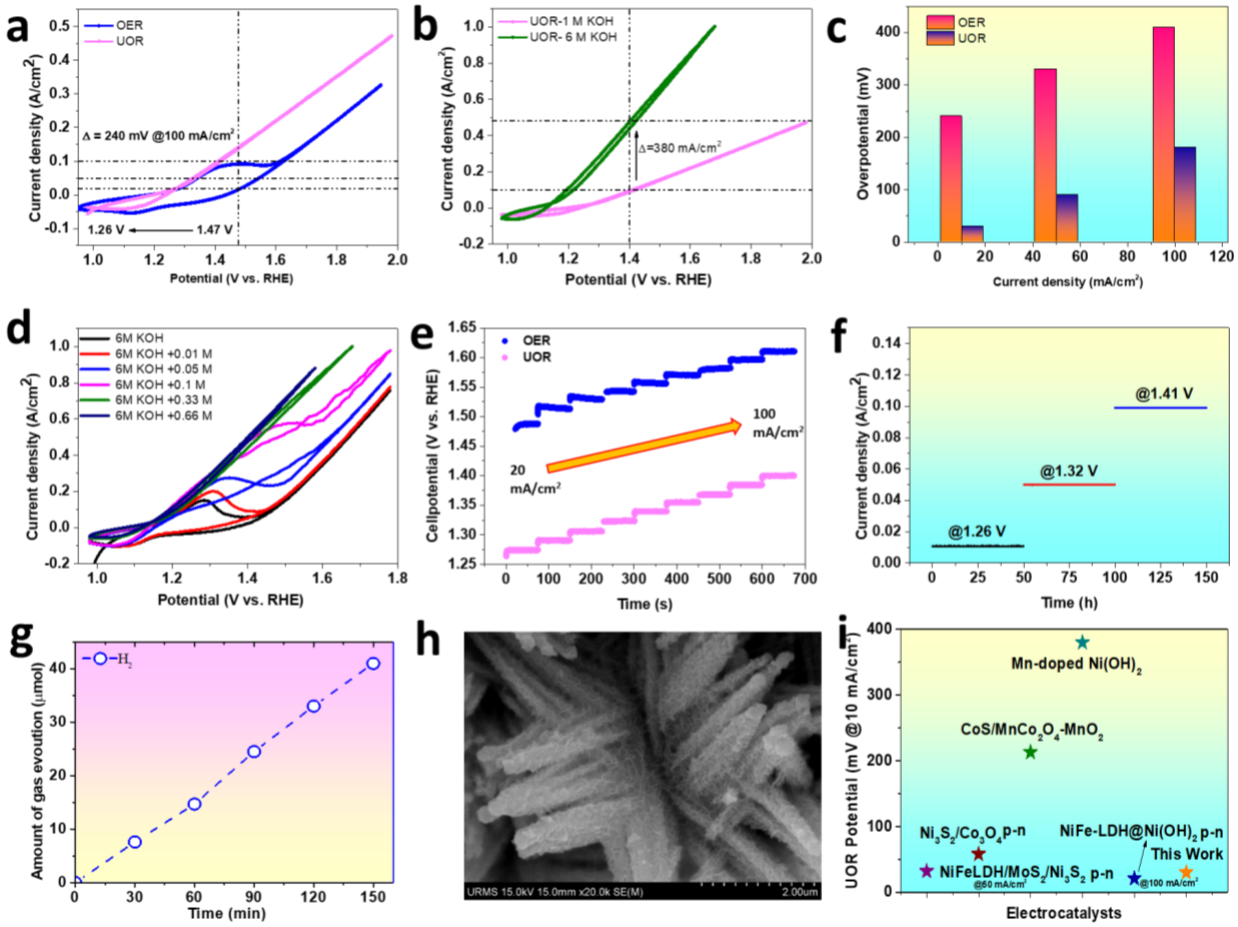

Figure 5. (a) Comparative OER and UOR (0.33 M Urea) with electrocatalyst MCONS3 electrode; (b) UOR performance with electrocatalyst MCONS3 electrode in 0.33 M + 1 M and 6 M KOH electrolyte; (c) comparative overpotentials for OER and UOR (0.33 M urea + 1 M KOH electrolyte); (d) effects of urea concentration (0.01, 0.05, 0.1, 0.33, and 0.66 M urea) on UOR performance in 6 M KOH electrolyte; (e) chronopotentiometry at different current densities versus time for OER and UOR with electrocatalyst MCONS3 electrode (0.33 M urea + 1 M KOH electrolyte); (f) stability tests of MCONS3 electrocatalyst electrode toward UOR in 1 M KOH electrolyte for 50 h @1.26 V, @1.32 V, and @1.41 V vs. RHE; (g) comparison of calculated and experimentally measured hydrogen gas with MCONS3 and Pt mesh electrode in 1 M KOH electrolyte with 0.33 M urea; (h) SEM image of MCONS3 after 50 h UOR stability test; (i) comparison of UOR potentials at 10 mA/cm^2 for various reported Mn, Co, and Ni based oxide and sulfide materials along with p-n heterojunction systems.

To gain some insights into the benefits of $MnCo_2O_{4.5}$@Ni_3S_2 compared to its two pure components, we performed density functional theory (DFT) computations. MCO was modeled as a defective bulk derived from $MnCo_2O_4$, i.e., as $Mn_7Co_{14}O_{32}$, i.e, $MnCo_2O_{4.57}$. The corresponding surface structure (010) was obtained from cleaving the constructed bulk. Both processes (introduction of defects and cleaving direction) were performed so as to minimize the energy of the resulting system. The structure of Ni_3S_2 was retrieved from Fleet, and the low-energy (110) surface was used. Finally, the model for $MnCo_2O_{4.5}$@Ni_3S_2 consists of a 2×1 unit cell of the MCO (010) surface covered by a 3×2 Ni_3S_2 (110) surface to minimize lattice mismatches. Based on these structural models, the minimal OER mechanisms involving three typical intermediates (OH*, O*, and OOH*) were investigated (**Figure 6a**). Since the initial adsorption of water on MCO was very exothermic, the surface is saturated with water molecules before computing the reaction profile (**Figure 6b-c**). As can be seen, MCO (blue lines) is expected to be an active OER catalyst: its onset potential is predicted to be around 1.4 V vs. RHE, with the oxidation of OH* to O* being the limiting step. In contrast, owing to the strong stabilization of O* on Ni_3S_2, this material is predicted to be subjected to surface oxidation, likely leading to NiOOH, a known OER catalyst. The same applies to $MnCo_2O_{4.5}$@Ni_3S_2 (orange line), where O* is even more strongly bound due to the lattice-mismatch-induced surface roughness of this catalyst. We explored this surface oxidation by adding more and more oxygen until further oxidation was not favorable anymore. Accordingly, we derived the surface model shown in **Figure 6d-e**. The corresponding OER reaction profile is shown in dark red in **Figure 6a**. We note that even on this highly oxidized surface, OH* is still exothermic while the formation of OOH* is incremental. By combining these two observations, there is strong indication that the experimentally observed OER activity may be due to in-situ formed extreme-surface NiOOH starting from Ni_3S_2 [36] [37]. Therefore, the role of each component in our p-n junctioned OER catalyst can be considered as follows: the NF provides mechanical stability and high electrical conductivity. Growing MCO over NF significantly increases the surface area and improves mass transport. Finally, the electrodeposition of Ni_3S_2 generates the precursor for a highly active NiOOH-like catalyst at the surface with a very high specific surface area.

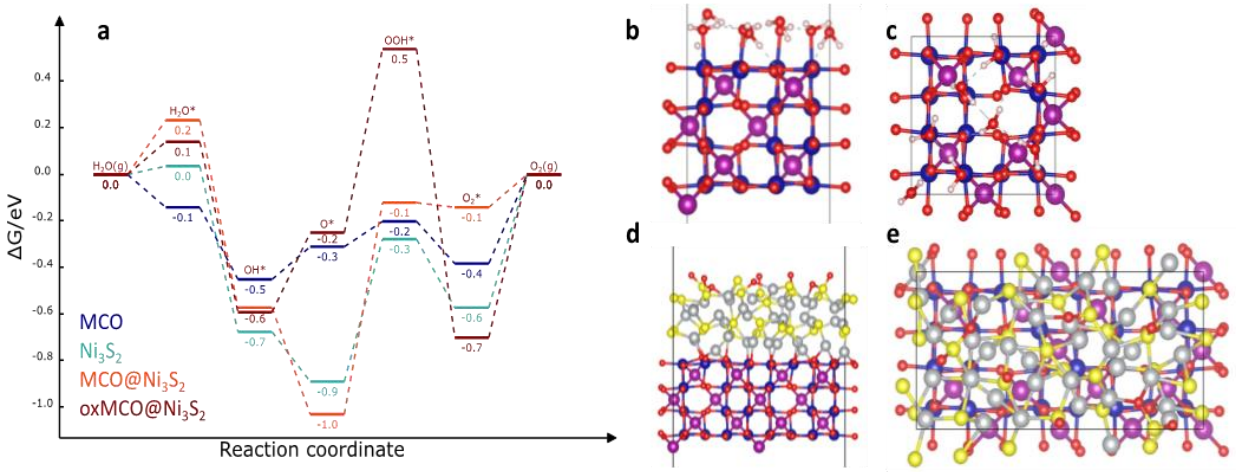

Figure 6. (a) OER reaction profile at 1.23 V vs. RHE on MCO (dark blue), Ni_3S_2 (teal), bare $MnCo_2O_{4.5}$@Ni_3S_2 (orange), and surface-oxidized $MnCo_2O_{4.5}$@Ni_3S_2 (dark red). (b) and (c) show side and top views of the structural model of MCO in water, while (d) and (e) show the side and top views of the structural model of the surface-oxidized $MnCo_2O_{4.5}$@Ni_3S_2.

Conclusion

In summary, the designed $MnCo_2O_{4.5}$@Ni_3S_2 p-n junction electrocatalyst exhibited enhanced electrochemical reactions and durability owing to the strong interfacial space charge region formed at p-n junction and additional support from the built-in-field promotes the electron transport with high stability. Under alkaline conditions, the lowest required overpotential for the OER and UOR were 1.47 V and 1.26 V vs. RHE at 10 mA/cm^2 current density and long term stable reactions till 50 h could be achieved. The electrocatalyst post-stability were observed partial composition changes. The in-situ formed amorphous NiOOH layer on the surface of Ni_3S_2 promotes the electrocatalytic activity as confirmed from DFT and post-TEM study. The high-efficiency heterogeneous electrocatalyst design not only hastens the sluggish OER kinetics but also accelerates the UOR process, potentially providing the means to solve the energy crisis and urea-contaminated wastewater treatment problems.

Acknowledgements

This work was supported by the National Research Foundation of Korea (NRF) (Grant No. 2022R1A2C2010803 and 2023K2A9A2A23000342). The authors thank the Korea Basic Science Institute (KBSI), Gwangju Center for the SEM and TEM analyses. Additionally, certain samples

underwent analysis through Scanning Electron Microscopy (SU5000/Hitachi) at the Energy Convergence Core Facility in Chonnam National University. SA thanks Architect Priyanjita Adhikari (National Institute of Design, Ahmedabad) for graphical illustrations. SNS thanks the SYSPROD project and AXELERA Pole de Competitivite for financial support (PSMN Data Center).

Conflict of interest

The authors declare no conflict of interest.

References:

[1] aS. J. Patil, N. R. Chodankar, S.-K. Hwang, G. S. Rama Raju, Y.-S. Huh, Y.-K. Han, *Small* **2022**, *18*, 2103326; bJ. Zhao, P. Xiao, *Korean Journal of Chemical Engineering* **2023**; cJ. Guo, N. Akram, L. Zhang, X. Cao, G. Wang, A. Ahmad, J. Niu, M. S. Mansha, Y. Zhang, J. Wang, *Korean Journal of Chemical Engineering* **2023**, *40*, 2751-2758; dT. Kavinkumar, H. Yang, A. T. Sivagurunathan, H. Jeong, J. W. Han, D.-H. Kim, *Small* **2023**, *19*, 2300963.

[2] aT. Li, H. C. Fu, X. H. Chen, F. Gu, N. B. Li, H. Q. Luo, *Journal of Colloid and Interface Science* **2022**, *618*, 196-205; bX. Du, Q. Wang, X. Zhang, Z. Wang, *International Journal of Hydrogen Energy* **2022**, *47*, 25595-25607; cA. T. Sivagurunathan, S. Seenivasan, T. Kavinkumar, D.-H. Kim, *Journal of Materials Chemistry A* **2024**, *12*, 4643-4655.

[3] L. Fei, H. Sun, R. Ran, W. Zhou, Z. Shao, *Industrial & Engineering Chemistry Research* **2021**, *60*, 1185-1193.

[4] A. Rebekah, S. Anantharaj, C. Viswanthan, N. Ponpandian, *International Journal of Hydrogen Energy* **2020**, *45*, 14713-14727.

[5] aJ. Li, S. Wang, J. Chang, L. Feng, *Advanced Powder Materials* **2022**, *1*, 100030; bR. P. Forslund, C. T. Alexander, A. M. Abakumov, K. P. Johnston, K. J. Stevenson, *ACS Catalysis* **2019**, *9*, 2664-2673.

[6] aS. Chen, C. Wang, S. Liu, M. Huang, J. Lu, P. Xu, H. Tong, L. Hu, Q. Chen, *The Journal of Physical Chemistry Letters* **2021**, *12*, 4849-4856; bY. Hu, T. Chao, Y. Li, P.

Liu, T. Zhao, G. Yu, C. Chen, X. Liang, H. Jin, S. Niu, W. Chen, D. Wang, Y. Li, *Angewandte Chemie International Edition* **2023**, *62*, e202308800.

[7] X. Zheng, J. Yang, P. Li, Z. Jiang, P. Zhu, Q. Wang, J. Wu, E. Zhang, W. Sun, S. Dou, D. Wang, Y. Li, *Angewandte Chemie International Edition* **2023**, *62*, e202217449.

[8] F. Shen, W. Jiang, G. Qian, W. Chen, H. Zhang, L. Luo, S. Yin, *Journal of Power Sources* **2020**, *458*, 228014.

[9] C. Santhosh, V. Velmurugan, G. Jacob, S. K. Jeong, A. N. Grace, A. Bhatnagar, *Chemical Engineering Journal* **2016**, *306*, 1116-1137.

[10] aG. Qian, J. Chen, L. Luo, H. Zhang, W. Chen, Z. Gao, S. Yin, P. Tsiakaras, *ACS Applied Materials & Interfaces* **2020**, *12*, 38061-38069; bJ. Liu, Y. Wang, Y. Liao, C. Wu, Y. Yan, H. Xie, Y. Chen, *ACS Applied Materials & Interfaces* **2021**, *13*, 26948-26959.

[11] aZ. Bai, J. Heng, Q. Zhang, L. Yang, F. Chang, *Advanced Energy Materials* **2018**, *8*, 1802390; bA. Rebekah, E. Ashok Kumar, C. Viswanathan, N. Ponpandian, *International Journal of Hydrogen Energy* **2020**, *45*, 6391-6403; cJ. Ge, W. Zhang, J. Tu, T. Xia, S. Chen, G. Xie, *Small* **2020**, *16*, 2001856; dH. Zhu, D. Yu, S. Zhang, J. Chen, W. Wu, M. Wan, L. Wang, M. Zhang, M. Du, *Small* **2017**, *13*, 1700468.

[12] X. Du, H. Su, X. Zhang, *International Journal of Hydrogen Energy* **2019**, *44*, 21637-21650.

[13] A. K. Shah, M. Qureshi, *ACS Applied Energy Materials* **2022**, *5*, 1551-1559.

[14] Y. Liu, X. Chi, Q. Han, Y. Du, J. Huang, X. Lin, Y. Liu, *Nanoscale* **2019**, *11*, 5285-5294.

[15] aM. Gu, L. Jiang, S. Zhao, H. Wang, M. Lin, X. Deng, X. Huang, A. Gao, X. Liu, P. Sun, X. Zhang, *ACS Nano* **2022**, *16*, 15425-15439; bY. Ma, Y. Zhang, M. Xing, S. Kang, M. Du, B. Qiu, Y. Chai, *Chemical Communications* **2022**, *58*, 6642-6645.

[16] P. Yi, Y. Song, Z. Liu, P. Xie, G. Liang, R. Liu, L. Chen, J. Sun, *Advanced Composites and Hybrid Materials* **2023**, *6*, 228.

[17] Y. Ma, C. Ma, Y. Wang, K. Wang, *Catalysts* **2022**, *12*, 337.

[18] aX. Wang, L. Xu, K. Song, R. Yang, L. Jia, X. Guo, X. Jing, J. Wang, *Colloids and Surfaces A: Physicochemical and Engineering Aspects* **2019**, *570*, 73-80; bS. Adhikari, Y. Kwon, D.-H. Kim, *Chemical Engineering Journal* **2020**, *402*, 126192.

[19] aZ. Xing, H. Wu, L. Wu, X. Wang, H. Zhong, F. Li, J. Shi, D. Song, W. Xiao, C. Jiang, F. Ren, *Journal of Materials Chemistry A* **2018**, *6*, 21167-21177; bX. Wang, L. Li, M. Shi, Y. Wang, G. Xu, K. Yuan, P. Zhu, M. Ding, Y. Chen, *Chemical Science* **2022**, *13*, 11639-11647.

[20] X. Wang, J. Wang, B. Yu, W. Jiang, J. Wei, B. Chen, R. Xu, L. Yang, *Journal of Hazardous Materials* **2022**, *428*, 128212.

[21] L. Sha, K. Ye, J. Yin, K. Zhu, K. Cheng, J. Yan, G. Wang, D. Cao, *Chemical Engineering Journal* **2020**, *381*, 122603.

[22] X. Du, J. Sun, R. Wu, E. Bao, C. Xu, H. Chen, *Nanoscale Advances* **2021**, *3*, 4447-4458.

[23] H. Rong, T. Chen, R. Shi, Y. Zhang, Z. Wang, *ACS Omega* **2018**, *3*, 5634-5642.

[24] J. Feng, H. Gao, L. Zheng, Z. Chen, S. Zeng, C. Jiang, H. Dong, L. Liu, S. Zhang, X. Zhang, *Nature Communications* **2020**, *11*, 4341.

[25] J. Yoon, W. Choi, T. Kim, H. Kim, Y. S. Choi, J. M. Kim, W.-S. Yoon, *Journal of Energy Chemistry* **2020**, *53*.

[26] S.-L. Kuo, J.-F. Lee, N.-L. Wu, *Journal of The Electrochemical Society* **2007**, *154*, A34-A38.

[27] B. Yang, Q. Han, L. Han, Y. Leng, T. O'Carroll, X. Yang, G. Wu, Z. Xiang, *Advanced Materials* **2023**, *35*, 2208661.

[28] F. H. Martins, F. G. Silva, F. L. O. Paula, J. de A. Gomes, R. Aquino, J. Mestnik-Filho, P. Bonville, F. Porcher, R. Perzynski, J. Depeyrot, *The Journal of Physical Chemistry C* **2017**, *121*, 8982-8991.

[29] C. Lan, H. Xie, Y. Wu, B. Chen, T. Liu, *Energy & Fuels* **2022**, *36*, 2910-2917.

[30] H. Liu, Q. He, H. Jiang, Y. Lin, Y. Zhang, M. Habib, S. Chen, L. Song, *ACS Nano* **2017**, *11*, 11574-11583.

[31] Y. Fu, H.-Y. Yu, C. Jiang, T.-H. Zhang, R. Zhan, X. Li, J.-F. Li, J.-H. Tian, R. Yang, *Advanced Functional Materials* **2018**, *28*, 1705094.

[32] T. Shinagawa, A. T. Garcia-Esparza, K. Takanabe, *Scientific Reports* **2015**, *5*, 13801.

[33] aY. Lu, W. Wang, F. Xie, *Journal of Electroanalytical Chemistry* **2020**, *871*, 114281; bT. ul Haq, S. A. Mansour, A. Munir, Y. Haik, *Advanced Functional Materials* **2020**, *30*, 1910309.

[34] aA. Abutaleb, *Catalysts* **2019**, *9*, 397; bR. M. Tesfaye, G. Das, B. J. Park, J. Kim, H. H. Yoon, *Scientific Reports* **2019**, *9*, 479.

[35] L. Liu, Y. Zhang, J. Wang, R. Yao, Y. Wu, Q. Zhao, J. Li, G. Liu, *International Journal of Hydrogen Energy* **2022**, *47*, 14422-14431.

[36] H. Ding, H. Liu, W. Chu, C. Wu, Y. Xie, *Chemical Reviews* **2021**, *121*, 13174-13212.

[37] Y.-F. Li, J.-L. Li, Z.-P. Liu, *The Journal of Physical Chemistry C* **2021**, *125*, 27033-27045.